Spatial metabolomics reveals localized impact of influenza virus infection on the lung tissue metabolome

Danya A. Dean,[a,b] London Klechka,[c] Ekram Hossain,[a,b] Adwaita R. Parab,[d] Krystin Eaton,[e] Myron Hinsdale,[e] Laura-Isobel McCall[a,b,d#]

[a]Department of Chemistry and Biochemistry, University of Oklahoma, Norman, Oklahoma

[b]Laboratories of Molecular Anthropology and Microbiome Research, University of Oklahoma, Norman, Oklahoma

[c]Department of Biology, University of Oklahoma, Norman, Oklahoma

[d]Department of Microbiology and Plant Biology, University of Oklahoma, Norman, Oklahoma

[e]Department of Physiological Sciences, Oklahoma State University, Stillwater, Oklahoma

#Address correspondence to Laura-Isobel McCall, lmccall@ou.edu

Running Head title: Spatial metabolomics of IAV infection

Abstract

The influenza virus (IAV) is a major cause of respiratory disease, with significant infection increases in pandemic years. Vaccines are a mainstay of IAV prevention, but are complicated by consideration of IAV's vast strain diversity, manufacturing and vaccine uptake limitations. While antivirals may be used for treatment of IAV, they are most effective in early stages of the infection and several virus strains have become drug resistant. Therefore, there is a need for advances in IAV treatment, especially host-directed, personalized therapeutics. Given the spatial dynamics of IAV infection and the relationship between viral spatial distribution and disease severity, a spatial approach is necessary to expand our understanding of IAV pathogenesis. We used spatial metabolomics to address this issue. Spatial metabolomics combines liquid chromatography-tandem mass spectrometry of metabolites extracted from systematic organ sections, 3D models and computational techniques, to develop spatial models of metabolite location and their role in organ function and disease pathogenesis. In this project, we analyzed plasma and systematically sectioned lung tissue samples from uninfected or infected mice. Spatial mapping of sites of metabolic perturbations revealed significantly lower metabolic perturbation in the trachea compared to other lung tissue sites. Using random forest machine learning, we identified metabolites that responded differently in each lung position based on infection, including specific amino acids, lipids and lipid-like molecules, and nucleosides. These results support the implementation of spatial metabolomics to understand metabolic changes upon IAV infection and to identify candidate pathways to be targeted for IAV therapeutics.

Importance

The influenza virus is a major health concern. Over 1 billion people become infected annually despite the wide distribution of vaccines, and antiviral agents are insufficient to address

43 current clinical needs. In this study, we used spatial metabolomics to understand changes in the
44 lung and plasma metabolome of mice infected with influenza A virus, compared to uninfected
45 controls. We determined metabolites altered by infection in specific lung tissue sites and
46 distinguished metabolites perturbed by infection between lung tissue and plasma samples. Our
47 findings highlight the importance of a spatial approach to understanding the intersection
48 between lung metabolome, viral infection and disease severity. Ultimately, this approach will
49 expand our understanding of respiratory disease pathogenesis and guide the development of
50 novel host-directed therapeutics.

51 **Introduction**

52 Influenza virus outbreaks are a continuous public health issue. Seasonal global
53 epidemics caused by both influenza A viruses (IAV) and influenza B viruses cause 300,000-
54 500,000 deaths each year (1). Vaccinations are the current method of prevention, but they fail to
55 account for every possible viral strain. Antiviral drugs are used for treatment of IAV but are most
56 effective within a short window during early infection. Additionally, it is believed that some
57 strains have developed resistance to these drugs (2). One study indicated that while influenza
58 A(H1N1)pdm09-infected intensive care unit patients treated with neuraminidase inhibitors have
59 greater survival rates than untreated patients, one in four treated patients still die (3). These
60 findings indicate a strong need for new treatments for IAV infection, and the potential for host-
61 targeted therapeutics to supplement antiviral agents. Their development, however, necessitates
62 an understanding of disease pathogenesis, which remains incompletely elucidated for IAV.

63 We used metabolomics to identify and analyze metabolites affected by IAV infection.
64 Metabolomics is a method of analysis that focuses on small molecules involved in biological
65 processes. This technique allows us to gain insight on the host chemical response to viral
66 infection. A comprehensive understanding of the relationship between host and virus could aid

67 in the development of more effective prevention and treatment options. Previous studies applied
68 metabolomic methods to lung tissue and serum during IAV infection. These studies found that
69 nucleosides such as uridine, lipids such as sphingosine, sphinganine, and amino acid
70 metabolites such as kynurenine are increased during infection in lung tissue (4). Additionally,
71 carbohydrates such as mannitol, myo-inositol and glyceric acid are decreased during active
72 infection. However, location of IAV within the respiratory tract is dynamic. Viral localization and
73 location of tissue damage within the respiratory tract also influences disease symptoms, disease
74 severity and transmissibility of the infection (5, 6, 7, 8). Thus, a spatial perspective is necessary
75 with regards to IAV and tissue metabolism. Chemical cartography is an approach that combines
76 liquid chromatography-mass spectrometry (LC-MS) with 3D visualizations, leading to detailed
77 spatial maps of metabolite distribution compared to pathogen load, tissue damage, or immune
78 responses (9, 10, 11). This approach, when applied to other infectious diseases enabled the
79 discovery of new treatments for these conditions (10). This method has been used to study the
80 impact of cystic fibrosis on the local lung metabolome (12, 13), but had not previously been
81 applied to IAV infection.

82 We therefore hypothesized that spatial metabolomics could provide new insights
83 regarding IAV infection. Using this method, we analyzed the distribution of small (*m/z* 100-
84 1,500) metabolites within the infected trachea and lung, in comparison to plasma samples and
85 to uninfected animals. We identified changes in the lung metabolome and determined limited
86 overlap in metabolites perturbed by IAV infection between lung tissue and plasma. Additionally,
87 we identified several metabolites altered by infection such as amino acids, lipids and lipid-like
88 molecules, and nucleosides. Interestingly, these metabolites were differentially affected at each
89 lung position. Ultimately, our study highlights the application of spatial metabolomics to
90 understand IAV infection and further our understanding of respiratory disease pathogenesis, to
91 guide the development of novel host-directed therapeutics.

Results

Viral distribution influences IAV transmissibility, viral reassortment and disease severity (5, 14, 15). While a few studies have investigated the changes in the metabolome during IAV infection, a spatial perspective of the metabolic disturbances is lacking (4, 16–18). We therefore used spatial metabolomics to identify candidate pathways and metabolites altered by infection in specific lung locations. Plasma, trachea and lungs were collected from IAV-infected mice at 3 days post-infection. Lungs were systematically sectioned into 11 segments (Fig. 1A), and all samples analyzed by liquid chromatography-tandem mass spectrometry (LC-MS/MS), followed by 3D reconstruction of metabolomics data. In addition, tissue homogenate bioluminescence was measured as an indicator of local viral burden in each tissue segment.

Using principal coordinate analysis (PCoA), we first compared lung and plasma metabolomes and found that the local lung tissue metabolome does not reflect the circulating metabolome (PERMANOVA <0.001, Fig 1D). Furthermore, lung tissue overall was found to be greatly impacted by infection (PERMANOVA <0.001, R^2 0.093931) (Fig 1E). A similar but non-significant, trend was seen between infected and uninfected plasma samples (Fig 1F).

Spatial analyses of lung tissue showed that viral load was largely localized to the lung tissue (positions 1-11) with minimal viral load in the trachea (position 12) (Dunn's test $p<0.05$, FDR-corrected, for comparisons between trachea and all positions except left lung middle (position 3, Fig 1B)). Overall local impact of infection on the metabolome was quantified using PERMANOVA R^2 at each sampling site. Magnitude of metabolic perturbation was variable between tissue segments, with the highest degree of metabolic perturbation in two segments of the left lung (position 1 and position 4), and the right lung middle lobe (position 8), whereas the trachea metabolome was least affected (R^2 range from 0.05 in trachea to 0.18 at position 4; Fig 1C and Table S15). Thus, sites of highest and lowest metabolic perturbation match sites with

116 high vs low viral load, respectively, enabling insight into the specific metabolites most affected
117 by infection.

118 We next sought to determine whether the specific metabolites perturbed by infection
119 differed between lung and plasma (Fig 1G-I). We used a random forest classifier, applied to
120 plasma on the one hand, and to lung tissue on the other hand (all positions combined). After
121 applying significance cutoffs (see Materials and Methods), this approach yielded a total list of 9
122 plasma metabolites and 374 lung tissue metabolites significantly perturbed by infection. There
123 was strikingly limited overlap of infection-perturbed metabolites between lung tissue samples
124 and plasma samples, indicating that both sites respond differentially to infection (Fig 1H) and
125 concurring with overall PCoA analysis findings (Fig 1D). We then sought to assess whether the
126 metabolites perturbed by infection were uniquely elicited by infection, or found under both
127 conditions but at differential levels. The majority of infection-perturbed metabolites were
128 common to infected and uninfected samples but found at different levels, with a minority
129 uniquely detected in uninfected samples only (Fig 1I). A similar trend was seen in infected and
130 uninfected plasma samples, where most infection-perturbed metabolites were present in both
131 infected and uninfected samples, albeit at different levels (Fig 1G). This signifies that the effect
132 of IAV infection on the metabolome is primarily on metabolite levels rather than induction of
133 novel metabolites.

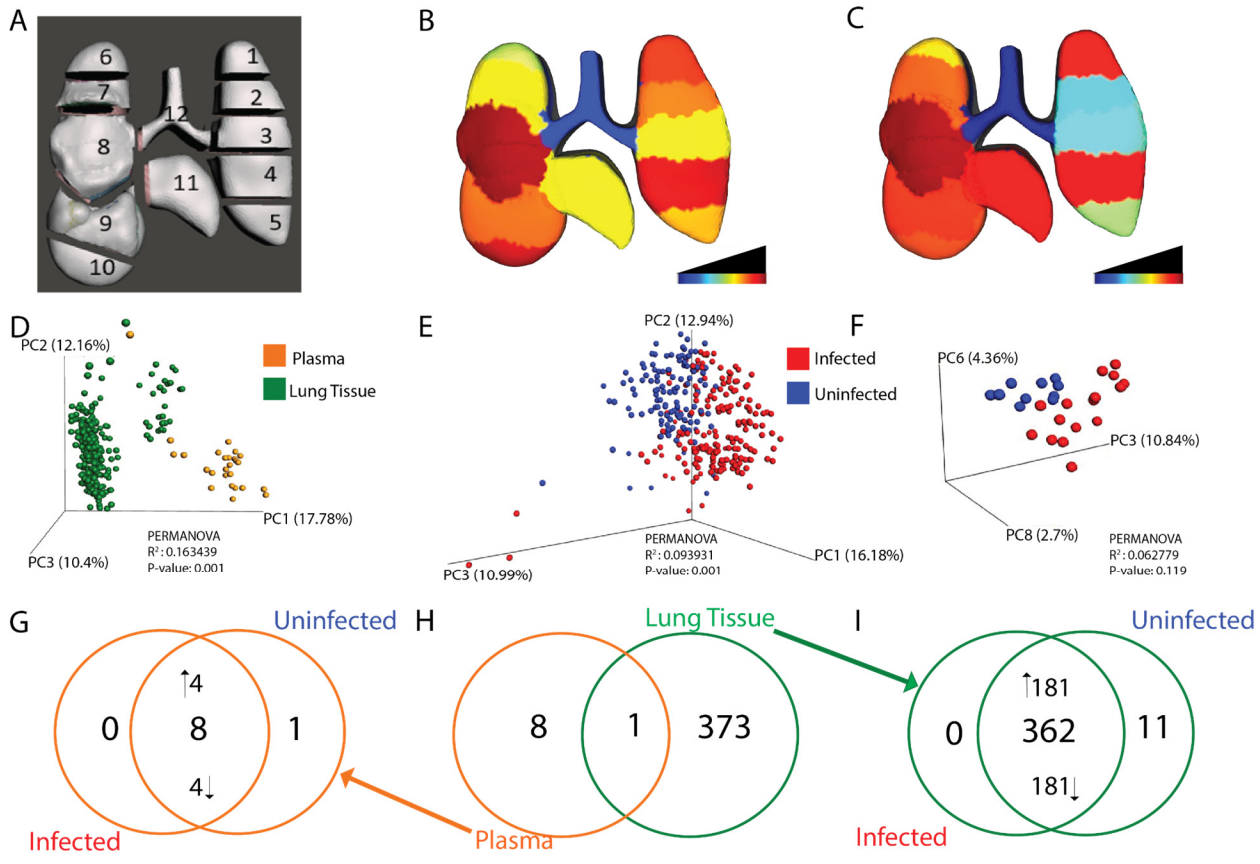

Figure 1. Localized impact of IAV infection in lung tissue and plasma. A: 3D model of lung tissue showing sampling positions. **B:** Median viral burden distribution of IAV. Lower infection levels were observed in the trachea (Dunn's test, FDR-corrected, $p<0.05$ for comparisons between trachea and all positions except left lung middle (position 3)). **C:** Magnitude of metabolic perturbation compared to uninfected (PERMANOVA R^2). **D:** Principal coordinate analysis (PCoA) plot showing differences in overall metabolome by sample type (PERMANOVA p-value <0.001). **E:** Impact of infection on overall lung tissue metabolome (PERMANOVA p-value <0.001). **F:** No significant impact of infection on the overall plasma metabolome by PCoA. **G-I:** Unique and common metabolites perturbed by infection **G:** Most metabolites perturbed by infection in plasma samples are found in both infected and uninfected samples, albeit at different levels. 4/8 metabolites were increased by infection and 4/8 were decreased by infection, while only one of the statistically significant metabolites was uniquely observed only in uninfected plasma samples. **H:** Overlap of metabolites perturbed by infection in plasma (orange) or lung tissue all positions combined (green). **I:** Most metabolites perturbed by infection in lung samples are found in both infected

148 and uninfected samples, albeit at different levels (181/382 metabolites increased by infection and 181/362
149 decreased by infection, with 11 of the statistically significant metabolites uniquely detected in uninfected
150 lung tissue).

151 Random forest classifier was also used to analyze the common and unique responses of
152 each lung and tracheal tissue site to infection. A random forest model was built for each lung
153 position and for plasma, classifying infected versus uninfected samples. Strikingly, most
154 infection-impacted metabolites were only affected at one or a few tissue sites (Fig 2A). This is
155 not due to divergence in overall metabolome between sites, as analysis of all metabolites,
156 irrespective of abundance, revealed large commonality across lung tissue sites and plasma (Fig
157 2B). Likewise, infection-perturbed metabolites do not overlap appreciably with metabolites
158 differing in abundance between lung and plasma (Fig S3). Very few perturbed metabolites were
159 identified for position 12 (trachea), perhaps as a consequence of the low viral load at that site
160 (Fig 1B).

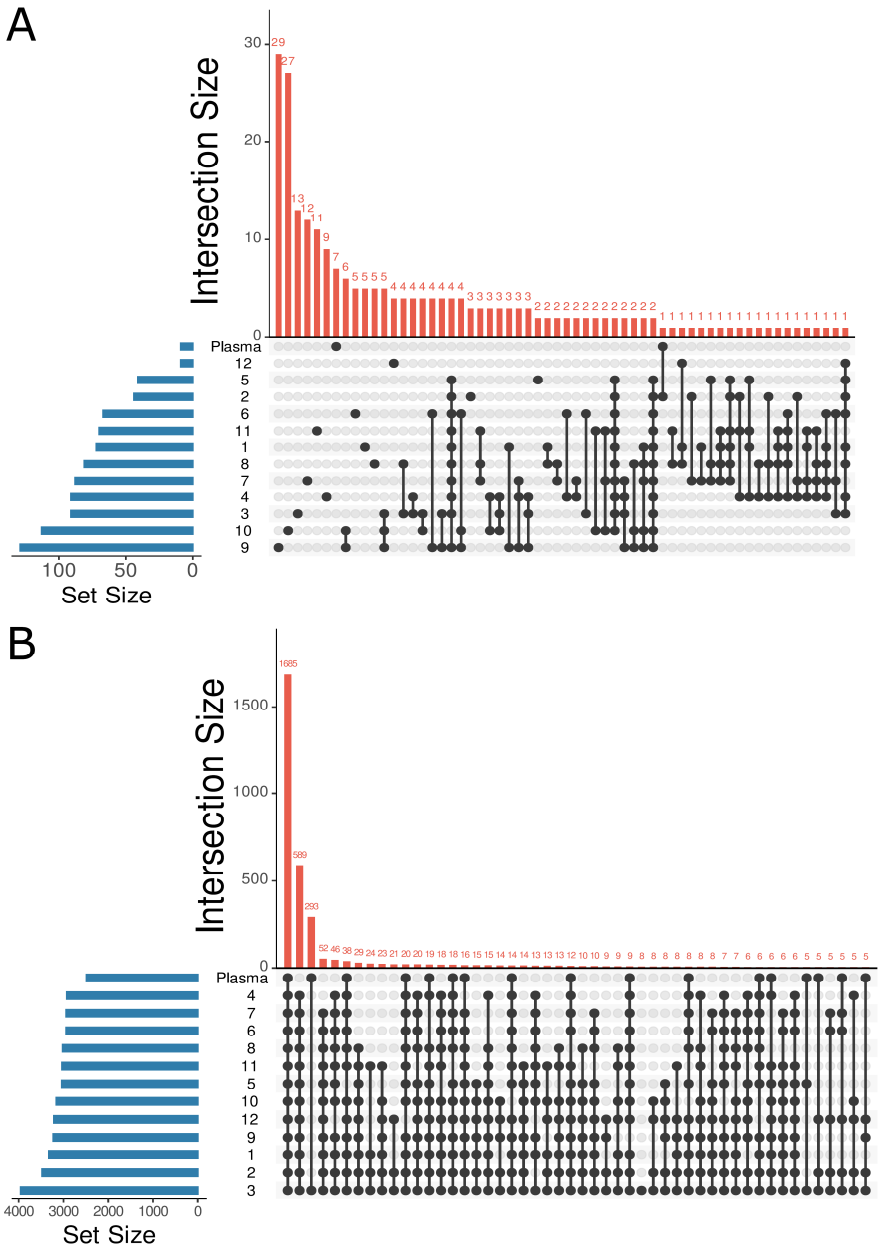

Figure 2: Location-specific impact of IAV infection on metabolism. A: UpSet plot (Number of intersections to show: 60) showing uniqueness of statistically significant infection-impacted metabolites in lung tissue and plasma perturbed, based on 13 random forest models analyzing each lung segment and plasma separately. B: UpSet plot (Number of intersections to show: 50) of total metabolites found in lung tissue and plasma showing large commonality across tissue sites and plasma. Position numbers as in Fig. 1A.

168 Metabolites perturbed by infection were annotated using molecular networking (19).
169 Among these, carnitine, glutamine, kynurenine, and cytosine were found to be significantly and
170 markedly perturbed by IAV infection and in a spatial manner (Fig 3, Fig S1). Glutamine,
171 cytosine, and kynurenine were all significantly increased by IAV infection at all tissue sites
172 except the trachea (Wilcoxon FDR-corrected p-value <0.05 at all sites except trachea) (Fig 3,
173 Fig S1). The opposite trend was seen for carnitine which was decreased by infection at all
174 tissue sites except the trachea (Wilcoxon FDR-corrected p-value <0.05 at all sites except
175 trachea) (Fig 3, Fig S1). In contrast, these metabolites were not significantly affected by
176 infection in the plasma.

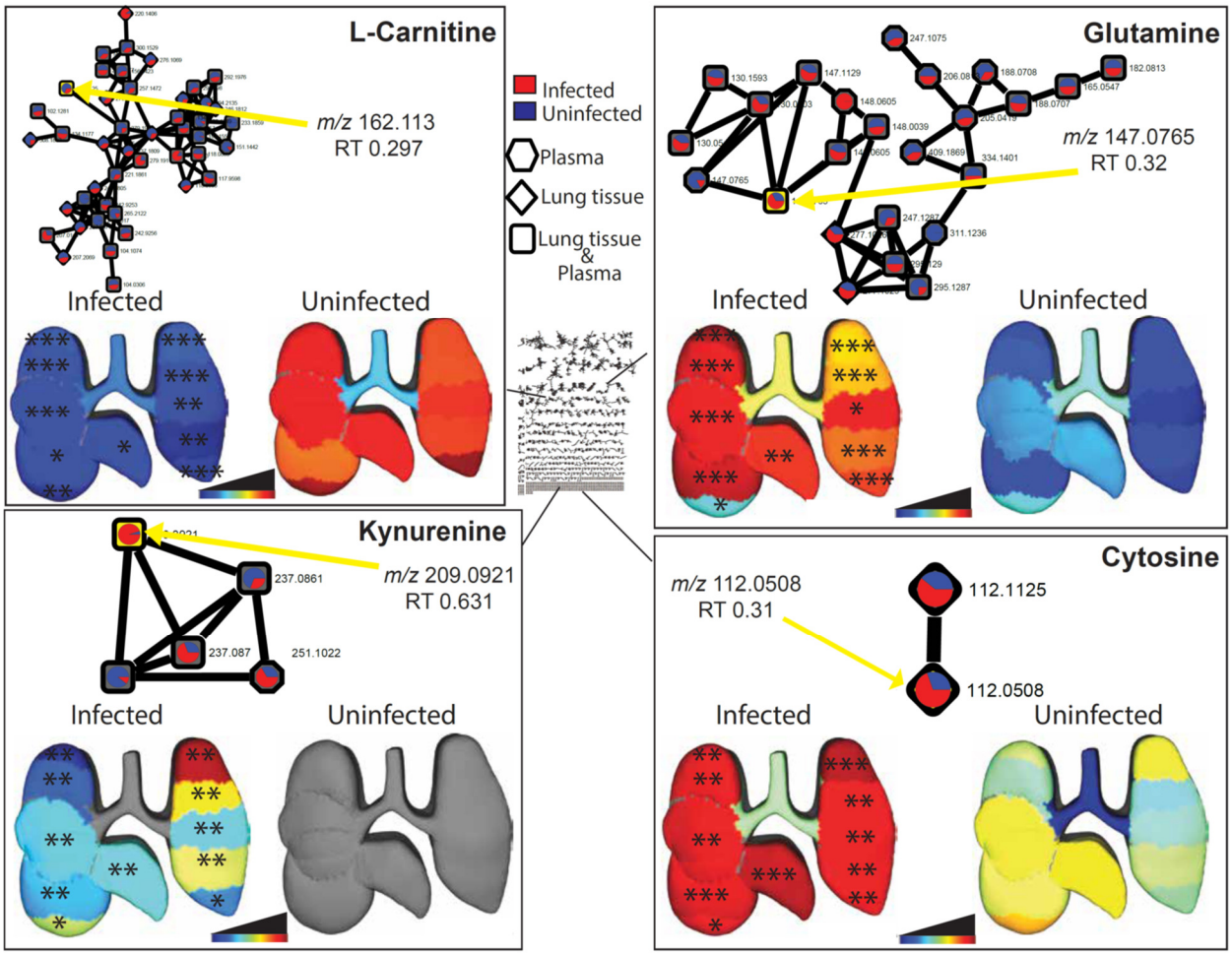

177

178 **Figure 3: Representative metabolites perturbed by IAV infection.** Molecular networks display
179 summed peak area of metabolites in infected (red) and uninfected (blue) samples. Each connected node
180 represents structurally-related metabolites, as determined by molecular networking. 3D lung 'ili plots show
181 median peak area of each displayed metabolite across tissue sites. Wilcoxon FDR-corrected p-values
182 comparing matched infected and uninfected lung tissue sites *<0.05; **<0.01; *** <0.001.

183 Additional metabolites perturbed by infection in plasma and lung tissue include amino
184 acids, acylcarnitines and nucleobases (Fig 4, Table S1, Table S2), with contrasting effects
185 between lung tissue positions and sample types. For example, amino acids had dissimilar
186 effects following IAV infection in plasma and lung tissue samples (Fig 4): methionine was
187 decreased in infected plasma samples (Wilcoxon FDR-corrected p-value <0.001) while
188 phenylalanine and L-citrulline were increased in infected lung tissue samples (Wilcoxon FDR-
189 corrected p-value <0.05) (Fig 4 A, E-F). However, the dipeptide methionine-phenylalanine was
190 decreased in infected lung tissue (Wilcoxon FDR-corrected p-value <0.05) (Fig 4K).
191 Acylcarnitines (oleylcarnitine and palmitoylcarnitine) were significantly increased in infected
192 plasma samples (Wilcoxon FDR-corrected p-value <0.001) compared to uninfected samples
193 (Fig 4B-C). Guanine, S-adenosy-homocyteine, spermidine, 4-hydroxynonenal, and hemin cation
194 were all significantly increased upon infection (Wilcoxon FDR-corrected p-value <0.05) at select
195 lung tissue sites (Fig 4F-H, G and L). Infection had the opposite effect on palmitamide, which
196 was significantly decreased in infected tissue samples (Fig 4I). In contrast, none of these
197 metabolites apart from phenylalanine were significantly affected by infection in the trachea.

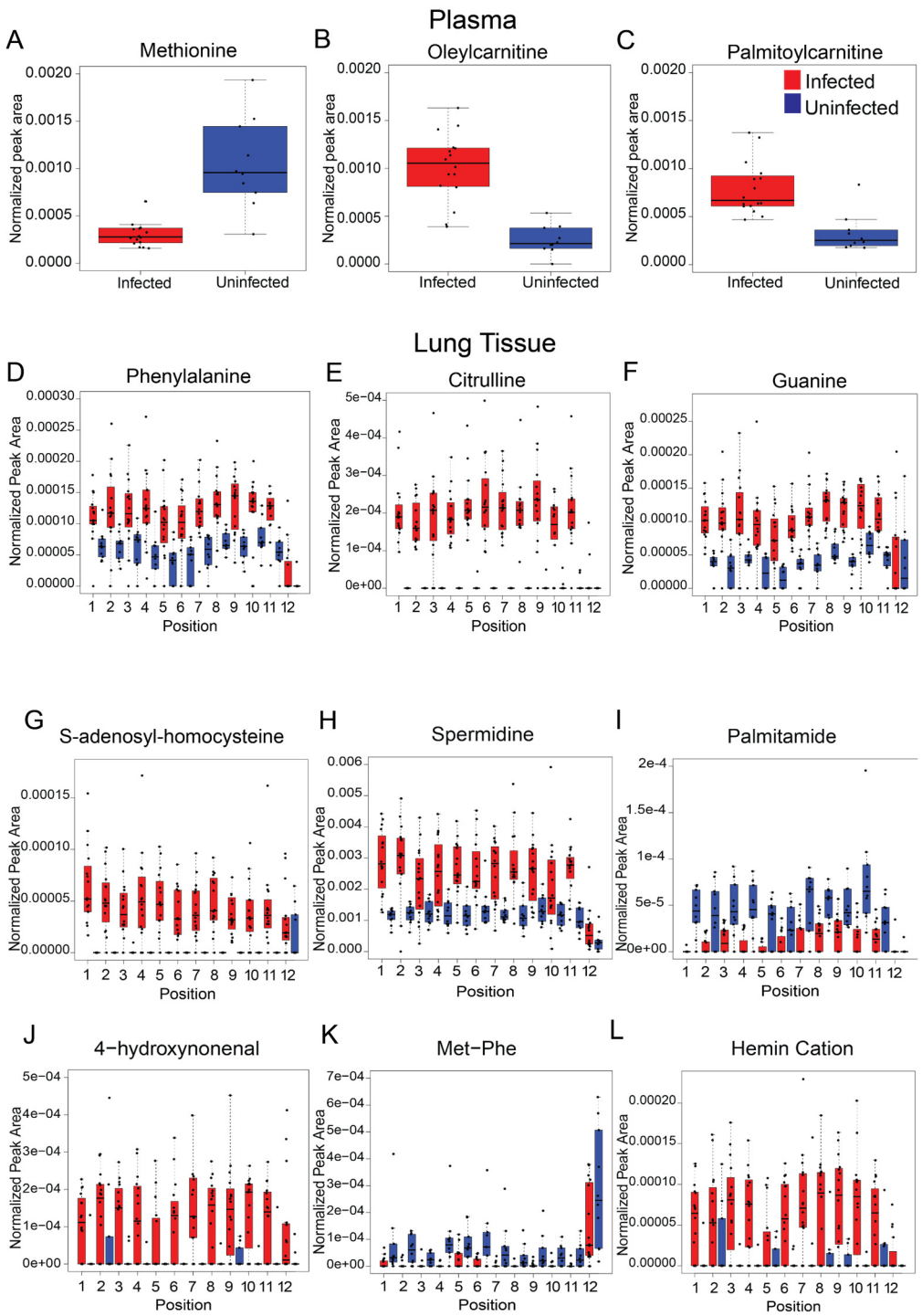

Fig 4: Representative metabolites perturbed by IAV infection in plasma and lung tissue. A-C: Statistically significant metabolites altered by infection in plasma (Wilcoxon FDR-corrected p-value <0.001). **A:** Methionine (*m/z* 150.058, RT 0.323 min). **B:** Oleyl L-carnitine (*m/z* 426.357, RT 2.982 min). **C:** Palmitoylcarnitine (*m/z* 400.341, RT 2.952 min). **D-L:** Statistically significant metabolites altered by

204 infection in lung tissue. **D:** Phenylalanine (*m/z* 166.042, RT 2.246 min) statistically different at all positions
205 (Wilcoxon FDR-Corrected p-value <0.05) except positions 2, 5, 10 and 12. **E:** Citrulline (*m/z* 198.085, RT
206 0.309 min) statistically significant at all positions (Wilcoxon FDR-Corrected p-value <0.05) except position
207 12. **F:** Guanine (*m/z* 150.977, RT 0.291 min) statistically different at all positions (Wilcoxon FDR-
208 Corrected p-value <0.05) except position 12. **G:** S-Adenosyl-homocysteine (*m/z* 385.212, RT 2.166 min)
209 statistically significant at all positions (Wilcoxon FDR-Corrected p-value <0.05) except position 12. **H:**
210 Spermidine (*m/z* 146.165, RT 0.287 min) statistically significant at all positions (Wilcoxon FDR-Corrected
211 p-value <0.05) except positions 3, 10, and 12. **I:** Palmitamide (*m/z* 256.073 RT 2.563 min) statistically
212 significant at all positions (Wilcoxon FDR-Corrected p-value <0.05) except positions 2, 5, 6, 7, 11, and 12.
213 **J:** 4-Hydroxynonenal (*m/z* 139.112, RT 2.644 min) statistically significant at all positions (Wilcoxon FDR-
214 Corrected p-value <0.05) except positions 1, 2, 3, 5, 11, and 12. **K:** Met-Phe (*m/z* 297.123, RT 2.444 min)
215 statistically significant at all positions (Wilcoxon FDR-Corrected p-value <0.05) except positions 3, 4, 6,
216 and 7. L: Hemin cation (*m/z* 616.358, RT 2.994 min) statistically significant at all positions (Wilcoxon FDR-
217 Corrected p-value <0.05) except positions 3, 4, 9, and 10.

218 **Discussion**

219 Here, we generated spatial maps of the metabolic impact of IAV infection on the mouse
220 lung and trachea. This approach revealed differential effects of infection across tissue sites and
221 between lung and plasma, as well as differential viral burden between trachea and lung tissue.
222 Based on random forest analysis and molecular networking, infection-impacted metabolites of
223 biological significance were annotated as acylcarnitines, amino acids, phospholipids, and
224 nucleotides, amongst others.

225 L-carnitine was significantly decreased by IAV infection at all lung positions except the
226 trachea (Fig 3 top left). Likewise, short chain acylcarnitines such as CAR 2:0 and CAR 6:0 were
227 also decreased in lung tissue (Table S3-14). In contrast, in both plasma and lung tissue,
228 different long chain acylcarnitines were increased by infection, including oleyl carnitine (CAR
229 18:1) and palmitoylcarnitine (CAR 16:0) in plasma and CAR 14:1 and CAR 20:1 in lung tissue

230 (Fig 4B-C, Table S1-14). Carnitines and acylcarnitines are key intermediates in energy
231 production via fatty acid beta oxidation, and influenza virus replication is sensitive to fatty acid
232 beta oxidation activity (20),(21). Likewise, these metabolic alterations may also be contributing
233 to the differential responses to vaccination in obese vs lean animals (22).

234 Our study indicated that glutamine is increased upon IAV infection (Fig 3 top right). T cell
235 proliferation and cytokine secretion relies heavily on glutamine presence (23). Thus, elevated
236 glutamine levels may enable anti-viral immunity IAV-infected cells are also more dependent on
237 glutamine availability than uninfected cells for survival, suggesting a pro-survival effect of our
238 observed elevated glutamine levels (24). Phenylalanine and citrulline were increased in infected
239 lung tissue, in contrast with methionine, which was decreased in plasma (Fig 4D-E). Both
240 phenylalanine and citrulline are involved in immune response by aiding in T-cell function (25).
241 Phenylalanine aids in activation of T-cells while citrulline has downstream effects through the
242 production of arginine which is used for T-cell growth and response (25–27). Upregulation of
243 both amino acids suggest their role in overall immune response to IAV.

244 Nucleotides, cytosine and guanine were elevated by infection in all lung sites except
245 trachea (Fig 3 bottom left and Fig 4F). Pyrimidine nucleotide biosynthesis is elevated upon IAV
246 infection, and indeed its replication was dependent on pyrimidine biosynthesis (28–30).
247 Interestingly, cytosine was found discriminatory in the plasma between RT-PCR positive COVID
248 patients and RT-PCR COVID negative patients (29).

249 Several of the metabolites annotated and identified as infection-impacted in the lung
250 tissue and plasma in this study are congruent with prior studies of respiratory infection (4).
251 Amino acids and nucleotides in particular were upregulated in lung tissue in other IAV studies
252 as well as in *Mycobacterium tuberculosis* infection (TB) and respiratory syncytial virus (RSV)
253 studies (4, 31–33). Phenylalanine was increased in mouse lung tissue in another IAV study and

254 in the serum and lung of mice infected with TB, while L-citrulline is elevated in mouse lung
255 tissue infected with RSV and in mice infected with TB (4, 17, 31, 32, 34). This coincides with our
256 findings showing elevations of these amino acids in IAV-infected lung tissue (Fig 4D and E).
257 Glutamine was identified in mouse lung tissue infected with TB and was elevated alongside
258 other immune response amino acids, corresponding with our study (Fig 3 top right) (32, 34).
259 Kynurenine, an infection-induced anti-inflammatory molecule, is consistently upregulated in
260 mouse lung tissue of several respiratory infection studies including TB, RSV, and our IAV study
261 (Fig 3 bottom left) (4, 31, 33, 34). Upregulation in cytosine in the lung tissue, oleylcarnitine in
262 plasma, and several phospholipids in the lung tissue are also consistent with current literature
263 (Fig 3 bottom right, Fig 4B and Table S1) (4, 17, 33).

264 Analysis of circulating metabolites has been performed in multiple studies on IAV
265 vaccinology (35), (36). Our findings of differential impact of infection on lung and plasma
266 metabolites (Fig. 1H, Table S1, Table S2) indicate that the metabolic changes observed in those
267 studies may not be directly linked to lung metabolic patterns, and this discrepancy was not due
268 purely to differences between plasma and lung overall (Fig. 2B). Likewise, the majority of
269 COVID-19 metabolomic studies have relied on serum or plasma samples (37). By extension,
270 based on this study's results, they may not be relevant to the pathogenesis of COVID-19 in the
271 lung, hampering translatability for drug development purposes. Thus, studies seeking to build on
272 metabolomics to design new treatments should rely on analysis of the affected organ, rather
273 than biofluids, even if the latter are more readily available.

274 We also observed differential impact of infection across lung sections, with the majority
275 of infection-perturbed metabolites only significantly perturbed at one lung segment (Fig. 2A).
276 The trachea in particular was especially divergent from the lung lobes in terms of viral burden
277 (Fig. 1B), overall magnitude of infection-induced metabolic perturbations (Fig. 1C) and specific

278 metabolic changes (Fig. 3, Fig. 4). Jointly, these results highlight the strength of our spatial
279 perspective.

280 As with any untargeted metabolomics studies, a significant fraction of infection-impacted
281 metabolites could not be annotated (~65%). The most commonly observed metabolite
282 subclasses in our dataset overall were amino acids, peptides, and analogues,
283 glycerophosphocholines, amines and fatty amides. Although this represents a broad diversity of
284 metabolite classes, nevertheless complementary metabolite extraction or data acquisition
285 methods could further expand this list. We further acknowledge that the mouse model of
286 influenza virus infection and mouse-adapted influenza viral strain may not be the most
287 representative of the functional lung alterations that would occur during human infection (38).
288 Indeed, the predominance of lower respiratory tract metabolic alterations over changes in the
289 trachea observed in this study. may be a consequence of this model. A further limitation is that
290 we focused on a single time point, in a lethal infection model. However, our findings serve as
291 proof-of-concept of the applicability of our approach to study respiratory viruses, with future
292 work applying this method in other biological systems.

293 We anticipate our findings to serve as a resource upon which the research community
294 can build to study the impact of different disease modifiers on the relationship between spatial
295 changes in the lung metabolome and disease severity, for example the impact of age,
296 comorbidities or treatment. Our findings and our approach also serve as a framework to study
297 how the metabolome is restored in a spatially-dependent fashion during recovery from
298 respiratory infection, or fails to recover during chronic disease in additional disease models, and
299 to identify markers of treatment response and infection outcome. Overall, we anticipate our
300 approach to be broadly applicable to many other respiratory infections, helping expand our
301 understanding of respiratory disease pathogenesis and to drive the development of host-
302 targeted therapeutic regimens.

303 **Materials and Methods**

304 ***In vivo* infection**

305 All vertebrate animal studies were performed under a protocol approved by Oklahoma
306 State University Institutional Animal Care and Use Committee (protocol number VM20-36), in
307 accordance with the USDA Animal Welfare Act and the Guide for the Care and Use of
308 Laboratory Animals of the National Institutes of Health.

309 Female C57BL/6J mice were anesthetized with ketamine and xylazine intraperitoneally
310 and then intranasally inoculated with PR8-Glu (39) (a generous gift from Dr. Peter Palese, Icahn
311 School of Medicine at Mount Sinai, Department of Microbiology, New York, New York, USA) at
312 2 X 10^3 pfu/mouse in 25-50 µl PBS. Controls were inoculated with PBS alone. Body weights
313 were monitored daily. Three days later, mice were anesthetized with ketamine and xylazine and
314 injected IV with a working solution of coelenterazine (GoldBio, St. Louis, Mo.) made according
315 to standard protocol (40). Briefly, using a stock solution of 7.5 mg/ml in acidified alcohol, each
316 mouse was administered 98 µg substrate in PBS (13 µl stock in 137 µl PBS) into the retroorbital
317 sinus. After substrate administration, the thoracic cavity was opened followed by exsanguination
318 by cardiac blood collection for serum and by lung tissue harvesting. Upper trachea, cranial to
319 tracheal bifurcation, was also collected. Subsequently, samples were submerged in
320 coelenterazine 0.3 mg/ml in a 96 well plate. Once collected the tissue pieces were blotted off
321 and flash frozen in liquid nitrogen for later analyses.

322 **Metabolite extraction and UHPLC-MS/MS**

323 A two-step metabolite extraction procedure was performed according to Want *et al.*(41)
324 for both tissue and plasma samples. Samples were homogenized in LC-MS grade water with
325 steel beads utilizing a Qiagen TissueLyzer at 25 Hz for 3 min, and 1 µl removed for
326 luminescence analysis. Methanol was added for a final concentration of 50%, samples

327 homogenized again for 3 mins and centrifuged at 16,000xg for 10 mins at 4ºC. The supernatant
328 (aqueous extract) was collected, dried overnight in a Speedvac and frozen at -80ºC until LC-MS
329 analysis. The pellet produced from centrifugation was collected for organic extraction via
330 addition of 3:1 dichloromethane:methanol, homogenized for 5 mins and centrifuged for 10 mins
331 at 4ºC. The organic extract was air dried overnight and then frozen at -80ºC until LC-MS
332 analysis. Dried aqueous and organic extracts were resuspended in 1:1 methanol and water
333 spiked with the internal standard sulfadimethoxine and combined. Samples were then
334 sonicated, centrifuged, and the supernatant collected for analysis. A Thermo Scientific Vanquish
335 UHPLC system was used for tissue and plasma analysis using a Kinetex 1.7µm C8 100 Å LC
336 column (50 x 2.1mm). Chromatography was done with water + 0.1% formic acid (mobile phase
337 A) and acetonitrile + 0.1% formic acid (mobile phase B), at a 0.5 mL/min flow rate (7.5 mins)
338 with a 40°C column temperature. LC gradient can be found in Table 1. Data acquisition was
339 performed in random sample order, with a blank and pooled quality control every 12 samples.
340 To monitor instrumental drift, a 6-mix solution with 6 known molecules was run at the beginning
341 and end of LC/MS/MS analysis. Calibration of the instrument was also done immediately prior to
342 instrument analysis using Pierce LTQ Velos ESI positive ion calibration solution. MS/MS
343 detection was conducted on a Q Exactive Plus (Thermo Scientific) high resolution mass
344 spectrometer (Table 2). Ions were generated for MS/MS analysis in positive mode.
345
346 Table 1: LC Gradient

Time(min)	Flow (ml/min)	%B	Curve
0.000	Run		
0.000	0.500	2.0	5
1.000	0.500	2.0	5
2.500	0.500	98.0	5

4.500	0.500	98.0	5
5.500	0.500	2.0	5
7.500	0.500	2.0	5
7.500	Stop Run		

347

348 Table 2: Q Exactive Plus (Thermo Scientific) instrument parameters

Runtime	0 to 7.5 min
Polarity	Positive
Default charge state	1
Full MS	
Resolution	70,000
AGC target	3e6
Maximum IT	246 ms
Scan range	100 to 1500 *m/z*
dd-MS2/dd-SIM	
Resolution	17,500
AGC target	1e5
Maximum IT	54 ms
Loop count	5
TopN	5
Isolation window	1.0 *m/z*
(N)ce/stepped (N)CE	NCE: 20, 40, 60
dd Settings	
Minimum AGC target	8.00e3
Intensity Threshold	1.5e5
Peptide match	preferred

Exclude isotopes	on
Dynamic exclusion	10.0s
Tune Data	
Spray Voltage (+)	3800.00
Capillary Temperature (+ or +-)	320.00
Sheath Gas (+ or +-)	35.00
Aux Gas (+ or +-)	10.00
Spare Gas (+ or +-)	0.00
Max Spray Current (+)	100.00
Probe Heater Temp (+ or +-)	0.00
S-Lens RF Level	50.00
Ion Source	HESI

349

350 **Luminescence analysis**

351 Coelenterazine was prepared according to GoldBio standard protocols. Briefly, 1 mg
352 coelenterazine was added to 1 mL of acidified methanol to make a stock solution. The stock
353 solution was made to a final concentration of 1.5 μM. A 1:10 solution of sample homogenate to
354 colentrazine was analyzed on a GloMax Explorer (Promega).

355 **LC-MS Data analysis**

356 Data analysis was performed using MZmine version 2.53, according to Table 3
357 parameters, to develop the feature table for further analysis. Blank removal with a 3-fold
358 threshold was performed and Jupyter notebooks were used to perform total ion current (TIC)
359 normalization. Principal coordinate analysis (PCoA) was performed on the TIC-normalized MS1
360 feature table using the Bray-Curtis dissimilarity metric in QIIME2 (42). Three-dimensional PCoA
361 plots were developed and visualized using EMPeror (43). Lung three-dimensional model

362 developed using Sketchup and Mesh lab, and modelling was completed using 'ili
363 (http://ili.embl.de/) (44).
364 Random forest analysis was conducted using R in Jupyter notebooks. Number of trees
365 were restricted to 500 and random forest classifier cutoff was based on variable importance
366 score of mean decrease accuracy >1. Lists were further restricted to FDR-corrected Mann-
367 Whitney p-value less than 0.05 and fold change <0.05 or >2.0. Venn diagrams and UpSet plots
368 were developed to quantify metabolite overlap within lung tissue positions and between lung
369 tissue and plasma using Intervene Shiny App (45).
370 Global Natural Products Social Molecular Networking (GNPS) was used to perform
371 feature-based molecular networking and MolNetEnhancer according to the parameters in Table
372 4. Cytoscape 3.8.2. was used to visualize all molecular networks. All reported annotations are at
373 Metabolomics Standards Initiative confidence level 2 (specific metabolite name provided) or
374 level 3 (metabolite family name provided only) (46). Lipids were annotated based on GNPS
375 library or analog matches, and using standard LipidMAPS nomenclature (47).
376
377 Table 3: MzMine 2.53 parameters

MS^1	
Retention Time (min)	0-7.5
Noise Level	5E5
MS^2	
Retention Time (min)	0-7.5
Noise Level	1E3
Chromatogram Builder	
Mass list	Masses
Minimum Time span (min)	0.01
Minimum Height	1.5E6

m/z Tolerance (ppm)	10.0
Algorithm	Baseline cut-off
Chromatogram Deconvolution	
m/z Range for MS² scan pairing (Da)	0.001
RT Range for MS² Scan pairing (min)	0.2
Minimum peak height	1.5E6
Peak duration range (min)	0-3.5
Baseline level	5E5
Deisotoping	
m/z tolerance (ppm)	10.0
Retention time tolerance (min)	0.5
Monotonic shape	Yes
Maximum Charge	3
Representative Isotope	Most intense
Alignment	
m/z Tolerance (ppm)	10.0
Weigh for *m/z*	1
Weight for Retention time	1
Retention time tolerance (min)	0.5
Row filtering	
Minimum peaks in a row	3
Retention time (min)	0.2-6.5
Keep only peaks with MS² scans	YES
Reset Peak No. ID	YES

380 Table 4: GNPS Parameters

Feature-Based Molecular Network	
Precursor Ion Mass Tolerance	0.02
Fragment Ion Mass Tolerance	0.02
Minimum Matched Fragment Ions	4
Maximum Connected Component Size (Beta)	100
Maximum shift between precursors	500
Library Search Min Matched Peaks	4
Search analogs	Do Search
Top results to report per query	1
Score Threshold	0.7
Maximum analog difference	100.0 Da
Minimum Peak Intensity	0.0
Filter Precursor Window	Filter
Filter peaks in 50 Da Window	Filter
Filter Library	Filter Library
Normalization per file	Row Sum Normalization (Per file Sum to 1,000,000)
Aggregation Method for peak abundances per group	Mean
PCoA	braycurtis
Run Dereplicator	Run

381

382 **Data availability:** All metabolomics data is publicly available in MassIVE under

383 accession number MSV000085389 (ftp://massive.ucsd.edu/MSV000085389).

384 MOLNet Enhancer link:

385 https://gnps.ucsd.edu/ProteoSAFe/status.jsp?task=f9f194c9b723409f8927c84470f9a0c5

386 Original GNPS link:

387 https://gnps.ucsd.edu/ProteoSAFe/status.jsp?task=bb7a5f7fb32045208b6040908a1453f7

388

389 **Acknowledgments**

390 This project was supported by a pilot grant from the Oklahoma Center for Respiratory
391 and Infectious Diseases (OCRID) under NIH award number P20GM103648 and used the
392 OCRID Animal Model Core, supported by the National Institute of General Medical Sciences
393 under award number P20GM103648. The authors further wish to acknowledge partial support
394 from NIH award number R21AI148886 and to thank Dr. Peter Palese, Icahn School of Medicine
395 at Mount Sinai, Department of Microbiology, New York, New York, USA, for providing the PR8-
396 Glu viral strain. Laura-Isobel McCall, Ph.D. holds an Investigators in the Pathogenesis of
397 Infectious Disease Award from the Burroughs Wellcome Fund. The content is solely the
398 responsibility of the authors and does not necessarily represent the official views of the National
399 Institutes of Health or any of the other funders.

400 **References**

401 1. Erbelding EJ, Post DJ, Stemmy EJ, Roberts PC, Augustine AD, Ferguson S, Paules CI,
402 Graham BS, Fauci AS. 2018. A Universal Influenza Vaccine: The Strategic Plan for the
403 National Institute of Allergy and Infectious Diseases. J Infect Dis 218:347–354.

404 2. 2012. Suppressing production of reactive oxygen species (ROS) for influenza A virus
405 therapy. Trends Pharmacol Sci 33:3–8.

406 3. Louie JK, Yang S, Acosta M, Yen C, Samuel MC, Schechter R, Guevara H, Uyeki TM.
407 2012. Treatment with neuraminidase inhibitors for critically ill patients with influenza A
408 (H1N1)pdm09. Clin Infect Dis 55:1198–1204.

409 4. Bernatchez JA, McCall L-I. 2020. Insights gained into respiratory infection pathogenesis

410 using lung tissue metabolomics. PLoS Pathog 16:e1008662.

411 5. Richard M, van den Brand JMA, Bestebroer TM, Lexmond P, de Meulder D, Fouchier RAM,
412 Lowen AC, Herfst S. 2020. Influenza A viruses are transmitted via the air from the nasal
413 respiratory epithelium of ferrets. Nat Commun 11:766.

414 6. van Riel D, Munster VJ, de Wit E, Rimmelzwaan GF, Fouchier RAM, Osterhaus ADME,
415 Kuiken T. 2007. Human and avian influenza viruses target different cells in the lower
416 respiratory tract of humans and other mammals. Am J Pathol 171:1215–1223.

417 7. Karlsson EA, Meliopoulos VA, Savage C, Livingston B, Mehle A, Schultz-Cherry S. 2015.
418 Visualizing real-time influenza virus infection, transmission and protection in ferrets. Nat
419 Commun 6:6378.

420 8. Tran V, Moser LA, Poole DS, Mehle A. 2013. Highly sensitive real-time in vivo imaging of
421 an influenza reporter virus reveals dynamics of replication and spread. J Virol 87:13321–
422 13329.

423 9. Dean DA, Gautham, Siqueira-Neto JL, McKerrow JH, Dorrestein PC, McCall L-I. Spatial
424 metabolomics identifies localized chemical changes in heart tissue during chronic cardiac
425 Chagas disease.

426 10. Hossain E, Khanam S, Dean DA, Wu C, Lostracco-Johnson S, Thomas D, Kane SS, Parab
427 AR, Flores K, Katemauswa M, Gosmanov C, Hayes SE, Zhang Y, Li D, Woelfel-Monsivais
428 C, Sankaranarayanan K, McCall L-I. 2020. Mapping of host-parasite-microbiome
429 interactions reveals metabolic determinants of tropism and tolerance in Chagas disease.
430 Sci Adv 6:eaaz2015.

431 11. McCall L-I, Morton JT, Bernatchez JA, de Siqueira-Neto JL, Knight R, Dorrestein PC,
432 McKerrow JH. 2017. Mass Spectrometry-Based Chemical Cartography of a Cardiac

433 Parasitic Infection. Anal Chem 89:10414–10421.

434 12. Garg N, Wang M, Hyde E, da Silva RR, Melnik AV, Protsyuk I, Bouslimani A, Lim YW,
435 Wong R, Humphrey G, Ackermann G, Spivey T, Brouha SS, Bandeira N, Lin GY, Rohwer
436 F, Conrad DJ, Alexandrov T, Knight R, Dorrestein PC. 2017. Three-Dimensional
437 Microbiome and Metabolome Cartography of a Diseased Human Lung. Cell Host Microbe
438 22:705–716.e4.

439 13. Melnik AV, Vázquez-Baeza Y, Aksenov AA, Hyde E, McAvoy AC, Wang M, da Silva RR,
440 Protsyuk I, Wu JV, Bouslimani A, Lim YW, Luzzatto-Knaan T, Comstock W, Quinn RA,
441 Wong R, Humphrey G, Ackermann G, Spivey T, Brouha SS, Bandeira N, Lin GY, Rohwer
442 F, Conrad DJ, Alexandrov T, Knight R, Dorrestein PC, Garg N. 2019. Molecular and
443 Microbial Microenvironments in Chronically Diseased Lungs Associated with Cystic
444 Fibrosis. mSystems 4.

445 14. Richard M, Herfst S, Tao H, Jacobs NT, Lowen AC. 2018. Influenza A Virus Reassortment
446 Is Limited by Anatomical Compartmentalization following Coinfection via Distinct Routes.
447 Journal of Virology.

448 15. Yan J, Grantham M, Pantelic J, Bueno de Mesquita PJ, Albert B, Liu F, Ehrman S, Milton
449 DK, EMIT Consortium. 2018. Infectious virus in exhaled breath of symptomatic seasonal
450 influenza cases from a college community. Proc Natl Acad Sci U S A 115:1081–1086.

451 16. Tisoncik-Go J, Gasper DJ, Kyle JE, Eisfeld AJ, Selinger C, Hatta M, Morrison J, Korth MJ,
452 Zink EM, Kim Y-M, Schepmoes AA, Nicora CD, Purvine SO, Weitz KK, Peng X, Green RR,
453 Tilton SC, Webb-Robertson B-J, Waters KM, Metz TO, Smith RD, Kawaoka Y, Suresh M,
454 Josset L, Katze MG. 2016. Integrated Omics Analysis of Pathogenic Host Responses
455 during Pandemic H1N1 Influenza Virus Infection: The Crucial Role of Lipid Metabolism. Cell

456 Host Microbe 19:254–266.

457 17. Cui L, Zheng D, Lee YH, Chan TK, Kumar Y, Ho WE, Chen JZ, Tannenbaum SR, Ong CN.
458 2016. Metabolomics Investigation Reveals Metabolite Mediators Associated with Acute
459 Lung Injury and Repair in a Murine Model of Influenza Pneumonia. Scientific Reports.

460 18. Milner JJ, Wang J, Sheridan PA, Ebbels T, Beck MA, Saric J. 2014. 1H NMR-based
461 profiling reveals differential immune-metabolic networks during influenza virus infection in
462 obese mice. PLoS One 9:e97238.

463 19. Wang M, Carver JJ, Phelan VV, Sanchez LM, Garg N, Peng Y, Nguyen DD, Watrous J,
464 Kapono CA, Luzzatto-Knaan T, Porto C, Bouslimani A, Melnik AV, Meehan MJ, Liu W-T,
465 Crüsemann M, Boudreau PD, Esquenazi E, Sandoval-Calderón M, Kersten RD, Pace LA,
466 Quinn RA, Duncan KR, Hsu C-C, Floros DJ, Gavilan RG, Kleigrewe K, Northen T, Dutton
467 RJ, Parrot D, Carlson EE, Aigle B, Michelsen CF, Jelsbak L, Sohlenkamp C, Pevzner P,
468 Edlund A, McLean J, Piel J, Murphy BT, Gerwick L, Liaw C-C, Yang Y-L, Humpf H-U,
469 Maansson M, Keyzers RA, Sims AC, Johnson AR, Sidebottom AM, Sedio BE, Klitgaard A,
470 Larson CB, P CAB, Torres-Mendoza D, Gonzalez DJ, Silva DB, Marques LM, Demarque
471 DP, Pociute E, O'Neill EC, Briand E, Helfrich EJN, Granatosky EA, Glukhov E, Ryffel F,
472 Houson H, Mohimani H, Kharbush JJ, Zeng Y, Vorholt JA, Kurita KL, Charusanti P, McPhail
473 KL, Nielsen KF, Vuong L, Elfeki M, Traxler MF, Engene N, Koyama N, Vining OB, Baric R,
474 Silva RR, Mascuch SJ, Tomasi S, Jenkins S, Macherla V, Hoffman T, Agarwal V, Williams
475 PG, Dai J, Neupane R, Gurr J, Rodríguez AMC, Lamsa A, Zhang C, Dorrestein K, Duggan
476 BM, Almaliti J, Allard P-M, Phapale P, Nothias L-F, Alexandrov T, Litaudon M, Wolfender J-
477 L, Kyle JE, Metz TO, Peryea T, Nguyen D-T, VanLeer D, Shinn P, Jadhav A, Müller R,
478 Waters KM, Shi W, Liu X, Zhang L, Knight R, Jensen PR, Palsson BO, Pogliano K,
479 Linington RG, Gutiérrez M, Lopes NP, Gerwick WH, Moore BS, Dorrestein PC, Bandeira N.

480 2016. Sharing and community curation of mass spectrometry data with Global Natural
481 Products Social Molecular Networking. Nat Biotechnol 34:828–837.

482 20. Longo N, Frigeni M, Pasquali M. 2016. Carnitine transport and fatty acid oxidation. Biochim
483 Biophys Acta 1863:2422–2435.

484 21. Munger J, Bennett BD, Parikh A, Feng X-J, McArdle J, Rabitz HA, Shenk T, Rabinowitz JD.
485 2008. Systems-level metabolic flux profiling identifies fatty acid synthesis as a target for
486 antiviral therapy. Nat Biotechnol 26:1179–1186.

487 22. Karlsson EA, Hertz T, Johnson C, Mehle A, Krammer F, Schultz-Cherry S. 2016. Obesity
488 Outweighs Protection Conferred by Adjuvanted Influenza Vaccination. MBio 7.

489 23. Carr EL, Kelman A, Wu GS, Gopaul R, Senkevitch E, Aghvanyan A, Turay AM, Frauwirth
490 KA. 2010. Glutamine uptake and metabolism are coordinately regulated by ERK/MAPK
491 during T lymphocyte activation. J Immunol 185:1037–1044.

492 24. Smallwood HS, Duan S, Morfouace M, Rezinciuc S, Shulkin BL, Shelat A, Zink EE, Milasta
493 S, Bajracharya R, Oluwaseum AJ, Roussel MF, Green DR, Pasa-Tolic L, Thomas PG.
494 2017. Targeting Metabolic Reprogramming by Influenza Infection for Therapeutic
495 Intervention. Cell Rep 19:1640–1653.

496 25. Sikalidis AK. 2015. Amino acids and immune response: a role for cysteine, glutamine,
497 phenylalanine, tryptophan and arginine in T-cell function and cancer? Pathol Oncol Res
498 21:9–17.

499 26. Lee Y-C, Su Y-T, Liu T-Y, Tsai C-M, Chang C-H, Yu H-R. 2018. L-Arginine and L-Citrulline
500 Supplementation Have Different Programming Effect on Regulatory T-Cells Function of
501 Infantile Rats. Front Immunol 9:2911.

502 27. Wijnands KAP, Castermans TMR, Hommen MPJ, Meesters DM, Poeze M. 2015. Arginine
503 and citrulline and the immune response in sepsis. Nutrients 7:1426–1463.

504 28. DeVito SR, Ortiz-Riaño E, Martínez-Sobrido L, Munger J. 2014. Cytomegalovirus-mediated
505 activation of pyrimidine biosynthesis drives UDP-sugar synthesis to support viral protein
506 glycosylation. Proc Natl Acad Sci U S A 111:18019–18024.

507 29. Blasco H, Bessy C, Plantier L, Lefevre A, Piver E, Bernard L, Marlet J, Stefic K, Benz-de
508 Bretagne I, Cannet P, Lumbu H, Morel T, Boulard P, Andres CR, Vourc'h P, Hérault O,
509 Guillon A, Emond P. 2020. The specific metabolome profiling of patients infected by SARS-
510 COV-2 supports the key role of tryptophan-nicotinamide pathway and cytosine metabolism.
511 Sci Rep 10:16824.

512 30. Hoffmann H-H, Kunz A, Simon VA, Palese P, Shaw ML. 2011. Broad-spectrum antiviral
513 that interferes with de novo pyrimidine biosynthesis. Proc Natl Acad Sci U S A 108:5777–
514 5782.

515 31. Sarkar I, Zardini Buzatto A, Garg R, Li L, van Drunen Littel-van den Hurk S. 2019.
516 Metabolomic and Immunological Profiling of Respiratory Syncytial Virus Infection after
517 Intranasal Immunization with a Subunit Vaccine Candidate. J Proteome Res 18:1145–1161.

518 32. Shin J-H, Yang J-Y, Jeon B-Y, Yoon YJ, Cho S-N, Kang Y-H, Ryu DH, Hwang G-S. 2011.
519 (1)H NMR-based metabolomic profiling in mice infected with Mycobacterium tuberculosis. J
520 Proteome Res 10:2238–2247.

521 33. Chandler JD, Hu X, Ko E-J, Park S, Lee Y-T, Orr M, Fernandes J, Uppal K, Kang S-M,
522 Jones DP, Go Y-M. 2016. Metabolic pathways of lung inflammation revealed by high-
523 resolution metabolomics (HRM) of H1N1 influenza virus infection in mice. Am J Physiol
524 Regul Integr Comp Physiol 311:R906–R916.

525 34. Fernández-García M, Rey-Stolle F, Boccard J, Reddy VP, García A, Cumming BM, Steyn
526 AJC, Rudaz S, Barbas C. 2020. Comprehensive Examination of the Mouse Lung
527 Metabolome Following Infection Using a Multiplatform Mass Spectrometry Approach. J
528 Proteome Res 19:2053–2070.

529 35. Zhou W, Sailani MR, Contrepois K, Zhou Y, Ahadi S, Leopold SR, Zhang MJ, Rao V, Avina
530 M, Mishra T, Johnson J, Lee-McMullen B, Chen S, Metwally AA, Tran TDB, Nguyen H,
531 Zhou X, Albright B, Hong B-Y, Petersen L, Bautista E, Hanson B, Chen L, Spakowicz D,
532 Bahmani A, Salins D, Leopold B, Ashland M, Dagan-Rosenfeld O, Rego S, Limcaoco P,
533 Colbert E, Allister C, Perelman D, Craig C, Wei E, Chaib H, Hornburg D, Dunn J, Liang L,
534 Rose SMS-F, Kukurba K, Piening B, Rost H, Tse D, McLaughlin T, Sodergren E, Weinstock
535 GM, Snyder M. 2019. Longitudinal multi-omics of host-microbe dynamics in prediabetes.
536 Nature 569:663–671.

537 36. Hagan T, Cortese M, Rouphael N, Boudreau C, Linde C, Maddur MS, Das J, Wang H,
538 Guthmiller J, Zheng N-Y, Huang M, Uphadhyay AA, Gardinassi L, Petitdemange C,
539 McCullough MP, Johnson SJ, Gill K, Cervasi B, Zou J, Bretin A, Hahn M, Gewirtz AT,
540 Bosinger SE, Wilson PC, Li S, Alter G, Khurana S, Golding H, Pulendran B. 2019.
541 Antibiotics-Driven Gut Microbiome Perturbation Alters Immunity to Vaccines in Humans.
542 Cell 178:1313–1328.e13.

543 37. Mussap M, Fanos V. 2021. Could metabolomics drive the fate of COVID-19 pandemic? A
544 narrative review on lights and shadows. Clin Chem Lab Med https://doi.org/10.1515/cclm-
545 2021-0414.

546 38. Thangavel RR, Bouvier NM. 2014. Animal models for influenza virus pathogenesis,
547 transmission, and immunology. Journal of Immunological Methods.

548 39. Heaton NS, Leyva-Grado VH, Tan GS, Eggink D, Hai R, Palese P. 2013. In vivo
549 bioluminescent imaging of influenza a virus infection and characterization of novel cross-
550 protective monoclonal antibodies. J Virol 87:8272–8281.

551 40. Tannous BA. 2009. Gaussia luciferase reporter assay for monitoring biological processes in
552 culture and in vivo. Nat Protoc 4:582–591.

553 41. Want EJ, Masson P, Michopoulos F, Wilson ID, Theodoridis G, Plumb RS, Shockcor J,
554 Loftus N, Holmes E, Nicholson JK. 2013. Global metabolic profiling of animal and human
555 tissues via UPLC-MS. Nat Protoc 8:17–32.

556 42. Caporaso JG, Kuczynski J, Stombaugh J, Bittinger K, Bushman FD, Costello EK, Fierer N,
557 Peña AG, Goodrich JK, Gordon JI, Huttley GA, Kelley ST, Knights D, Koenig JE, Ley RE,
558 Lozupone CA, McDonald D, Muegge BD, Pirrung M, Reeder J, Sevinsky JR, Turnbaugh
559 PJ, Walters WA, Widmann J, Yatsunenko T, Zaneveld J, Knight R. 2010. QIIME allows
560 analysis of high-throughput community sequencing data. Nat Methods 7:335–336.

561 43. Vázquez-Baeza Y, Pirrung M, Gonzalez A, Knight R. 2013. EMPeror: a tool for visualizing
562 high-throughput microbial community data. Gigascience 2:16.

563 44. Protsyuk I, Melnik AV, Nothias L-F, Rappez L, Phapale P, Aksenov AA, Bouslimani A,
564 Ryazanov S, Dorrestein PC, Alexandrov T. 2018. 3D molecular cartography using LC-MS
565 facilitated by Optimus and ’ili software. Nat Protoc 13:134–154.

566 45. Khan A, Mathelier A. 2017. Intervene: a tool for intersection and visualization of multiple
567 gene or genomic region sets. BMC Bioinformatics.

568 46. Sumner LW, Amberg A, Barrett D, Beale MH, Beger R, Daykin CA, Fan TW-M, Fiehn O,
569 Goodacre R, Griffin JL, Hankemeier T, Hardy N, Harnly J, Higashi R, Kopka J, Lane AN,
570 Lindon JC, Marriott P, Nicholls AW, Reily MD, Thaden JJ, Viant MR. 2007. Proposed

571 minimum reporting standards for chemical analysis. Metabolomics.

572 47. Fahy E, Sud M, Cotter D, Subramaniam S. 2007. LIPID MAPS online tools for lipid

573 research. Nucleic Acids Res 35:W606–12.

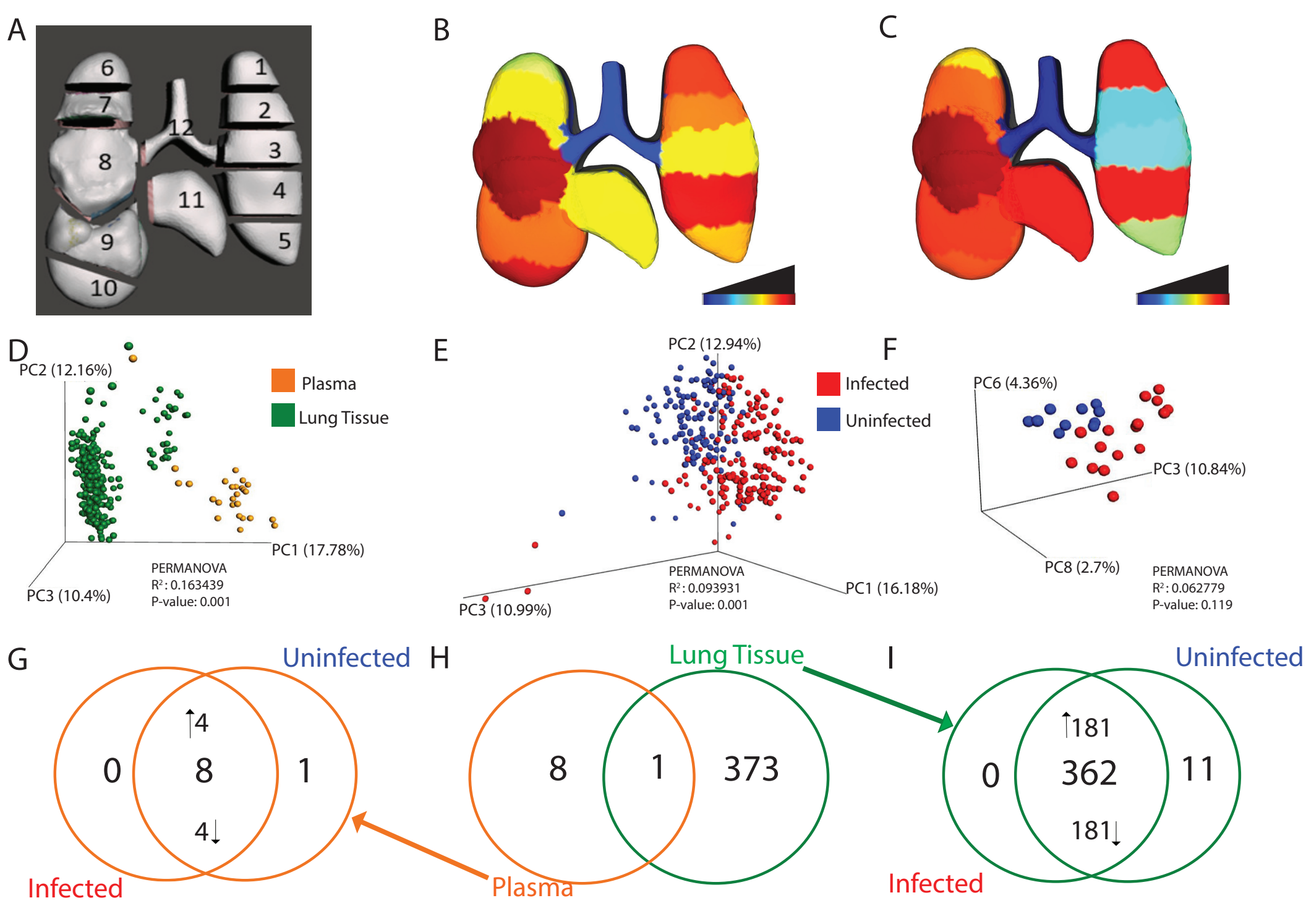
A
6
7
8
9
10
12
11
1
2
3
4
5
B
C
D
PC2 (12.16%)
Plasma
Lung Tissue
PC1 (17.78%)
PC3 (10.4%)
PERMANOVA
R²: 0.163439
P-value: 0.001
E
PC2 (12.94%)
Infected
Uninfected
PC3 (10.99%)
PERMANOVA
R²: 0.093931
P-value: 0.001
PC1 (16.18%)
F
PC6 (4.36%)
PC3 (10.84%)
PC8 (2.7%)
PERMANOVA
R²: 0.062779
P-value: 0.119
G
Uninfected
↑4
0
8
1
4↓
Infected
H
Lung Tissue
8
1
373
Plasma
I
Uninfected
↑181
0
362
11
181↓
Infected

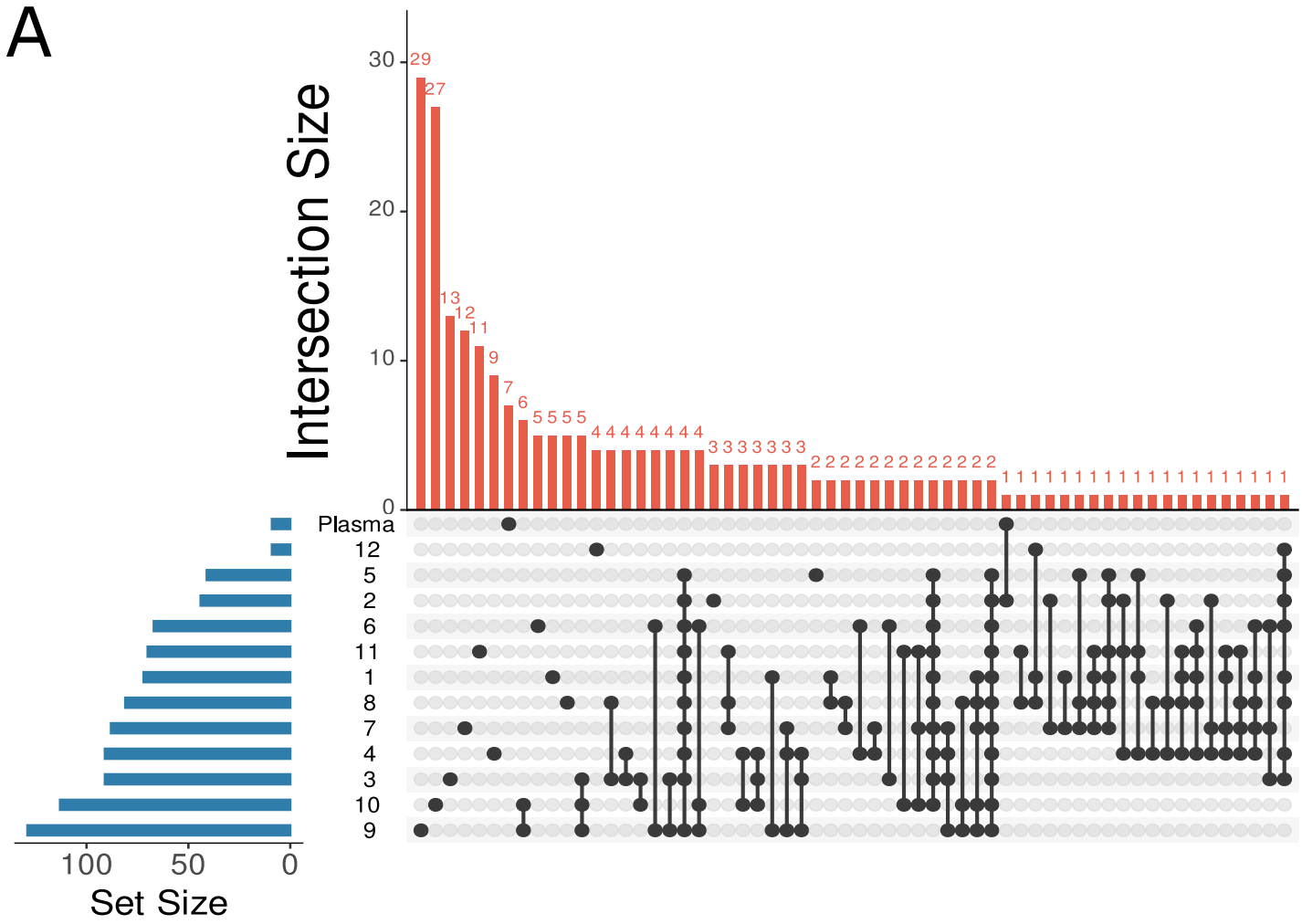
A
Intersection Size
30
20
10
0
29
27
13
12
11
9
7
6
5 5 5 5
4 4 4 4 4 4 4 4
3 3 3 3 3 3 3
2 2 2 2 2 2 2 2 2 2 2 2 2
1 1 1

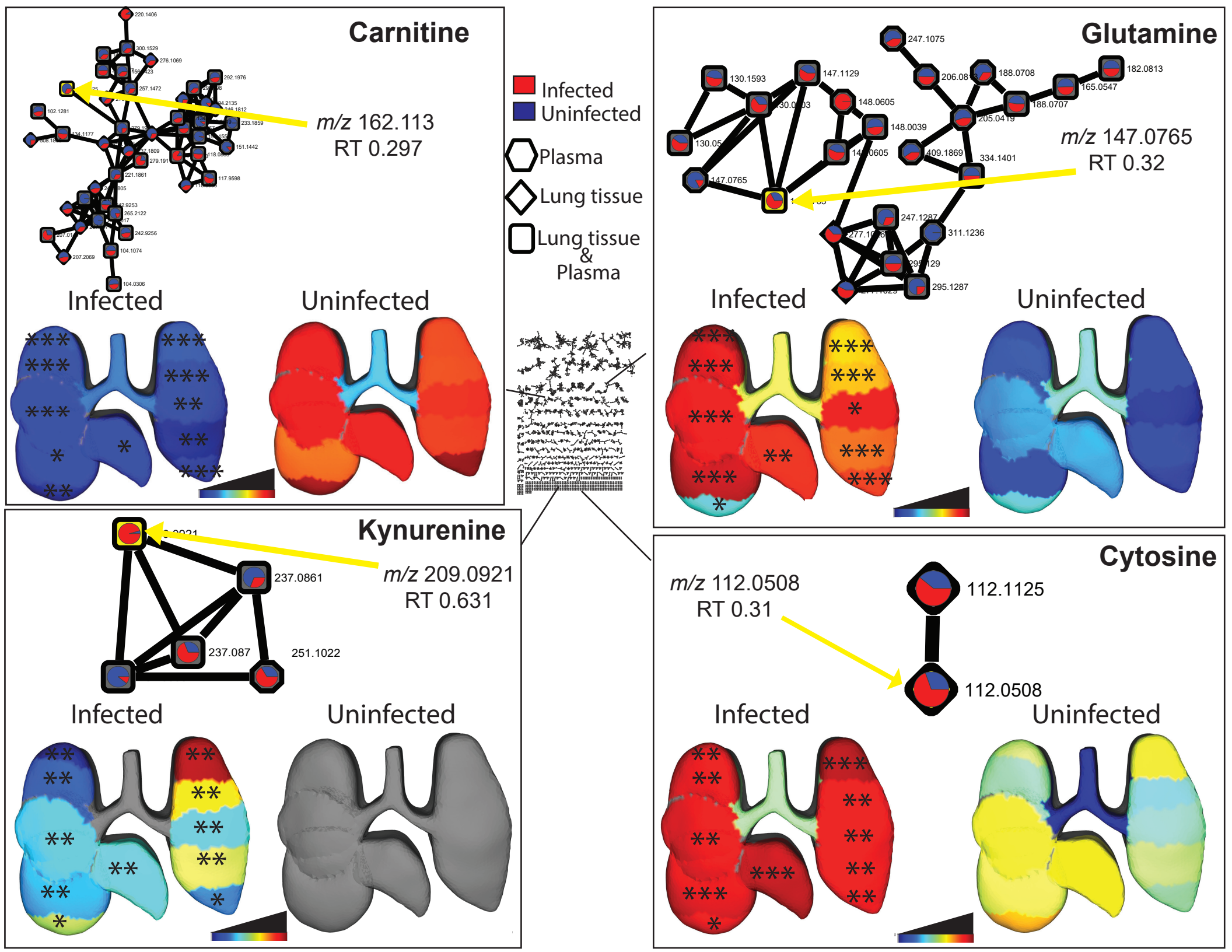
Carnitine
m/z 162.113
RT 0.297
Infected
Uninfected
Glutamine
m/z 147.0765
RT 0.32
Infected
Uninfected
Infected
Uninfected
Plasma
Lung tissue
Lung tissue & Plasma
Kynurenine
m/z 209.0921
RT 0.631
237.0861
237.087
251.1022
Infected
Uninfected
Cytosine
m/z 112.0508
RT 0.31
112.1125
112.0508
Infected
Uninfected

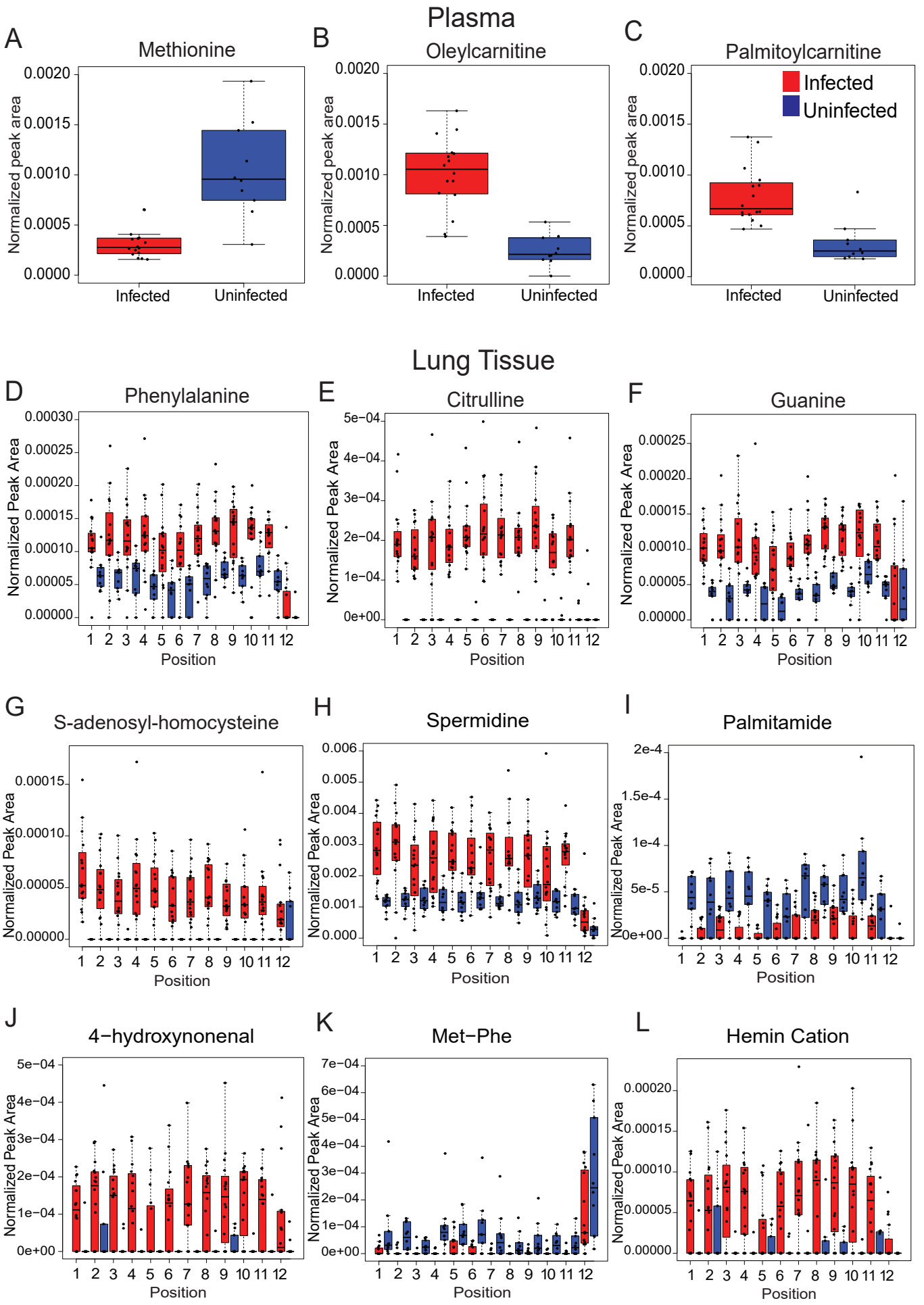
Plasma
A
Methionine
B
Oleylcarnitine
C
Palmitoylcarnitine
Infected
Uninfected
Normalized peak area
Lung Tissue
D
Phenylalanine
E
Citrulline
F
Guanine
G
S-adenosyl-homocysteine
H
Spermidine
I
Palmitamide
J
4−hydroxynonenal
K
Met−Phe
L
Hemin Cation
Normalized Peak Area
Position